

Transient, Three-dimensional, Multiscale Simulations of the Human Aortic Valve

Eli J. Weinberg · Mohammad Reza Kaazempur Mofrad

© Springer Science+Business Media, LLC 2007

Abstract A set of multiscale simulations has been created to examine the dynamic behavior of the human aortic valve (AV) at the cell, tissue, and organ length scales. Each model is fully three-dimensional and includes appropriate nonlinear, anisotropic material models. The organ-scale model is a dynamic fluid-structure interaction that predicts the motion of the blood, cusps, and aortic root throughout the full cycle of opening and closing. The tissue-scale model simulates the behavior of the AV cusp tissue including the sub-millimeter features of multiple layers and undulated geometry. The cell-scale model predicts cellular deformations of individual cells within the cusps. Each simulation is verified against experimental data. The three simulations are linked: deformations from the organ-scale model are applied as boundary conditions to the tissue-scale model, and the same is done between the tissue and cell scales. This set of simulations is a major advance in the study of the AV as it allows analysis of transient, three-dimensional behavior of the AV over the range of length scales from cell to organ.

Keywords Human aortic valve · Calcific aortic stenosis · Multiscale mechanics · Finite element modeling · Cell mechanics · Tissue mechanics · Organ biomechanics

E. J. Weinberg
Department of Mechanical Engineering, Massachusetts Institute of Technology, Cambridge, MA, USA

E. J. Weinberg
Draper Laboratory, Cambridge, MA, USA

E. J. Weinberg · M. R. Kaazempur Mofrad (✉)
Department of Bioengineering, University of California, Berkeley, CA 94720, USA
e-mail: mofrad@berkeley.edu

Introduction

Biological processes in both the healthy and diseased aortic valve (AV) occur over a range of length scales. Cells within the valve cusps, the valvular interstitial cells (VICs), are understood to sense and respond to mechanical stimuli. The VICs are subjected to transient deformations due to the organ-scale motion of the valve opening and closing. Currently, we understand that in healthy valves the transient deformations regulate appropriate matrix-maintaining functions of the VICs (Taylor et al. 2003). In diseased states, particularly in calcified valves, it is thought that abnormal mechanical signals lead to VIC dysfunction (Otto 2002). Additionally, calcification of bioprosthetic valves is believed to be a local effect of cusp deformation. As the health and repair of heart valves is of great clinical importance, significant research has been conducted to examine the mechanical behavior of the AV at each length scale.

The organ-scale motion of the AV has historically attracted significant attention from experimental and theoretical groups. Over the past three decades, many methods have been employed to monitor the motion of the AV. Its small size and rapid motion make measurements challenging, but imaging technologies have recently demonstrated the acquisition speed and resolution to discern valve motion (Baumert et al. 2005; Boehm et al. 2007). Earlier efforts have measured valve motion using surgically attached linear transducers (Brewer et al. 1977) and radio-opaque markers (Deck et al. 1988; Thubrikar et al. 1980, 1986), stereophotogrammetry (Clark et al. 1974), and silicone casting (Cataloglu et al. 1976, 1977; Gould et al. 1973).

A number of groups have used finite-element modeling to simulate the motion of the AV. There are two main

challenges in creating a finite-element simulation of a heart valve. First, the leaflets undergo large displacements through the blood, making remeshing of a fluid domain difficult for a coupled fluid-structure interaction. While fluid-structure interactions are generally approached using the arbitrary Lagrange–Eulerian coupling scheme, we are not aware of any work that successfully applies this method to a three-dimensional (3D) valve simulation. The second challenge in simulating valve motion is that the material is anisotropic and nonlinear. Kim et al. (2006, 2007) have modeled the valve motion with a specifically derived material model, but without the fluid phase. De Hart et al. (2003a, b, 2004) have implemented a fictitious domain method for coupling the fluid and solid without remesh of the fluid domain, and they have used this method to simulate the motion of the AV cusps with a fiber-supported constitutive material model. The finite element package LS-DYNA (LSTC, Livermore CA) includes the operator-splitting method which similarly couples solid to fluid without remeshing the fluid domain (Hallquist 2006). This software has been used to perform fluid-structure interactions of the AV, including the motion of the aortic root, with an anisotropic linear elastic material model (Nicosia et al. 2003) and to simulate the mitral valve with a user-defined fibrous material model (Einstein et al. 2004, 2005). A number of groups have simulated the valve solid without fluid or under quasistatic conditions. Sun provides a full list of such efforts (Sun et al. 2005).

A large body of research also exists in the measurement and simulation of the mechanical properties of AV tissue. The planar stress–strain behavior of complete tissue (Billiar and Sacks 2000a; Clark et al. 1974; Rousseau et al. 1983) and individual layers (Sacks and Yoganathan 2007; Vesely and Noseworthy 1991) have been measured as has the flexural stiffness of the tissue (Gloeckner et al. 1999). Merryman et al. (2006a) have measured the effect of cellular contraction on the overall tissue material properties. Various appropriate constitutive models have been formulated (Billiar and Sacks 2000b; Holzapfel et al. 2000) and implemented in solid and shell finite elements (Kim et al. 2007; Sun and Sacks 2005; Weinberg and Kaazempur-Mofrad 2005, 2006).

Modeling of cell-scale deformations in general is an active area of research (Lim et al. 2006; Mofrad and Kamm 2006), but investigations specific to the VICs are in the preliminary stages. Merryman et al. have measured the stiffness of VICs (Merryman et al. 2006b) and Huang et al. have computed the deformation of VICs in valves subjected to static pressure (Huang 2004).

While the mechanical behavior of the AV at the various length scales is a subject of wide interest, and multiscale analysis of other systems has been performed (Chandran and Barocas 2007; Migliavacca et al. 2006), as of yet no

effort has been made to cohesively bring together studies of the AV over the range from cellular to organ length scales. Understanding of all these processes will be greatly enhanced by a cohesive framework for examining the deformations of the AV at the various length scales. In this paper, we introduce a system of reference configurations to link the length scales. We describe finite-element simulations of AV mechanics at the cell, tissue, and organ length scales. Each simulation considers the transient, three-dimensional case with appropriate material models and geometry. The complete set of simulations enables unprecedented analysis of the AV mechanical behavior across the range of length scales needed to examine biological processes in the valve.

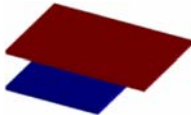
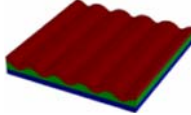
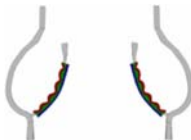
Methods

Multiscale Approach

Simulations were created to describe behaviors at the cell, tissue, and organ length scales. One challenge in describing AV mechanics is that the tissue goes through a wide range of deformations and these deformations may be referred to a range of reference configurations. Stella (Stella and Sacks 2007) and Billiar (Billiar and Sacks 2000b) have demonstrated the large difference in results possible when different reference configurations are assumed. In order to coherently link our simulations, we have defined a set of reference configurations. Our configuration definitions extend those of Stella (Stella and Sacks 2007; Sacks and Yoganathan 2007). These configurations are summarized in Table 1. In Ω_0 , the ventricularis and fibrosa are unattached and stress-free. The layers are connected to form the assembled tissue Ω_1 . In Ω_2 , the tissue is in position in a valve to which no pressure has been applied. When the valve is pressurized to its resting physiological state, the tissue is in Ω_3 . We denote the time-varying state of the tissue in the functioning valve as Ω_t .

The leaflet tissue exhibits locking behavior, where the stress needed to extend the tissue increases rapidly beyond some point. We define the extensibility of the tissue to be the stretch that can be applied to the tissue before the Cauchy stress exceeds 200 kPa in the direction of application. The extensibility of the leaflet tissue in each reference configuration, in both the circumferential and radial directions, can be determined from published experiments. The measured extensibilities of individual layers referred to Ω_0 are listed in Table 1 (Sacks and Yoganathan 2007). Stella's data show an increase in radial extensibility for the fibrosa from Ω_0 to Ω_1 . This increase is most likely due to the fibrosa being compacted into a wrinkled shape. We include the wrinkling effect in our

Table 1 Tissue reference configurations

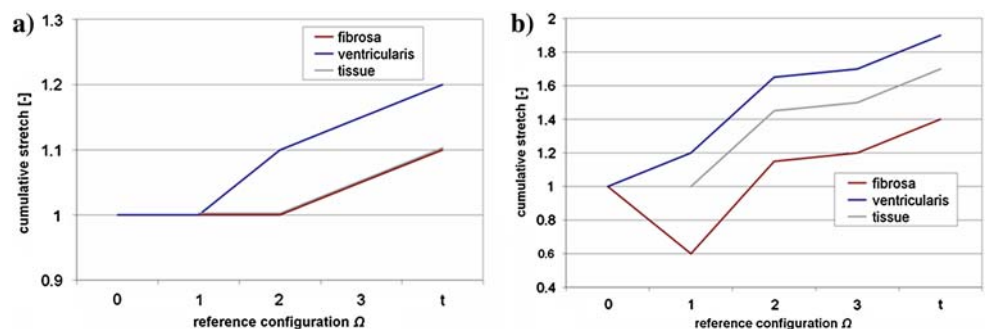
Symbol	Schematic	Description	Extensibilities
Ω_0		Unattached layers	Fibrosa: $\lambda_C = 1.10$, $\lambda_R = 1.40$ Ventricularis: $\lambda_C = 1.20$, $\lambda_R = 1.90$
Ω_1		Assembled tissue	Fibrosa: $\lambda_C = 1.10$, $\lambda_R = 1.40$ Ventricularis: $\lambda_C = 1.20$, $\lambda_R = 1.70$ Tissue: $\lambda_C = 1.10$, $\lambda_R = 1.70$
Ω_2		Tissue in valve with no external forces applied	Tissue: $\lambda_C = 1.10$, $\lambda_R = 1.25$
Ω_3		Tissue in valve with baseline pressure applied	Tissue: $\lambda_C = 1.05$, $\lambda_R = 1.20$
Ω_4		Tissue in functioning valve	Tissue, mid-diastole: $\lambda_C = 1.00$, $\lambda_R = 1.00$

models, so we assume that the fibrosa material has the same radial extensibility Ω_1 as in Ω_0 . The extensibilities of the assembled tissue referred to Ω_1 were estimated to be 1.7 in the radial direction and 1.2 in the circumferential direction (Billiar and Sacks 2000a). The extensibilities referred to the valve configuration Ω_2 are determined by assuming that the tissue reaches its locking stretches in both directions in diastole. The stretches at diastole have been measured (Cataloglu et al. 1977; Thubrikar 1990) to be 1.25 in the radial direction and 1.1 in the circumferential direction. The extensibilities referred to Ω_3 are not known a priori. For illustrative purposes, we assume that a small

stretch (1.05) is applied to the tissue in both directions between Ω_2 and Ω_3 . The magnitude of the stretch occurring between Ω_2 and Ω_3 will be calculated in the organ-scale simulation (see Section “Organ-level Simulation”).

Once the extensibilities are known, we can calculate the stretches that are applied to the tissue between each configuration. With those stretches, we can begin at any configuration and calculate the stretches required to reach any other configuration. In Fig. 1, the stretches required to move from Ω_0 to all other configurations in sequence are plotted. Note that a large stretch in the radial direction between Ω_1 and Ω_2 is required to reconcile the measured

Fig. 1 Cumulative stretches required to reach any configuration starting at Ω_0



extensibility of completely load-free tissue (Billiar and Sacks 2000a) with the observed extensibility of tissue in a functioning valve (Cataloglu et al. 1977; Thubrikar 1990). Thus, we are assuming that leaflet tissue, in an AV with no external forces applied, has tension in the radial direction. The stretch less than 1 in the radial direction for the fibrosa represents the wrinkling of this layer when the fibrosa and ventricularis are attached to each other.

We create our multiscale simulations within the framework of these reference configurations. For each simulation, a reference configuration is chosen and the simulation geometry and constitutive models are referred to that configuration. The simulations are listed in Table 2 with their length scales, reference configurations, and the configurations that they span.

These simulations are interfaced by a simple one-way coupling, passing data from the largest scale to the smallest. First, the organ-level simulation is run. Element strains output from the organ-level simulation are applied as boundary conditions to the tissue-level simulation. Then strains from the tissue-level simulation are passed similarly to the cell-level simulations.

Organ-level Simulation

The organ-level simulation was performed in LS-DYNA. This software was chosen because its operator-splitting method for fluid-structure interaction has been demonstrated to readily handle the motion of a solid through fluid typical of heart valve function (Einstein et al. 2004; Nicosia et al. 2003). LS-DYNA is an explicit solver, which means it may require excessive computation times in modeling relatively low-speed physical systems such as the AV. We address this issue in our formulation of the constitutive model used to describe the cusp tissue mechanics.

To simulate the cusp mechanics, we have developed a constitutive model that describes the bulk material behavior and is particularly computationally efficient in explicit finite element implementations. Like many tissue constitutive models (Billiar and Sacks 2000b; Holzapfel et al. 2000; Humphrey 2003, Sun and Sacks 2005), ours treats the tissue as an isotropic solid with embedded aligned fibers. Instead of using a continuum model, though, we take

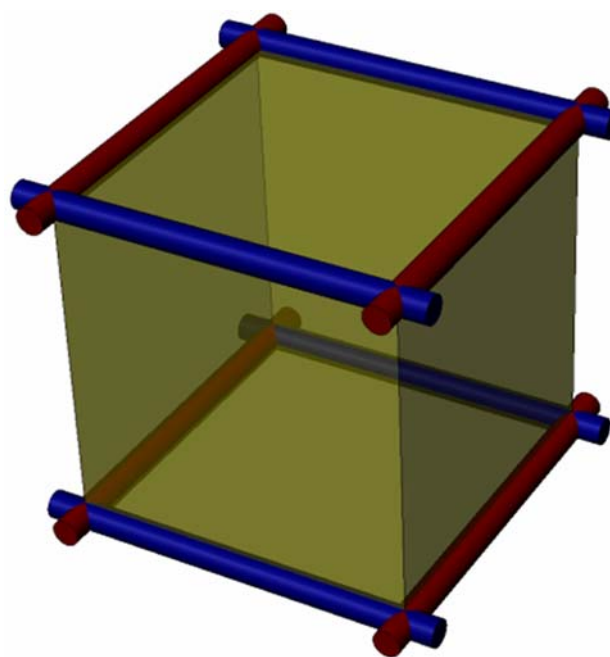


Fig. 2 Single solid element with two perpendicular fiber families

a discrete approach. The solid mesh elements are modeled with an isotropic material. One-dimensional cable elements are then used to connect the nodes of the solid element. LS-DYNA allows assignment of arbitrary stress–strain curves to the cable elements, and fiber rotations follow nodal displacements. A single element with this model is illustrated in Fig. 2. Red cylinders represent fibers of one family and blue represent fibers of another family, perpendicular to the first.

Appropriate stress–strain curves and cross-sectional areas must be chosen for each fiber. It is assumed that the fibers contribute no stiffness in compression. There is some flexibility in choosing the magnitude of the stresses and the cross-sectional area of the fibers. If an element with fibers along each edge is extended in a direction parallel to those fibers, the stress contribution of the fibers to total element response is

$$\sigma_c = \frac{4\sigma_f A_f}{A_e}, \quad (1)$$

where σ_f is the stress in each fiber, A_f is the cross-sectional area of each fiber, and A_e is the cross-sectional area of the solid element. Thus, σ_c should have a value corresponding to measured tissue properties and A_e is determined by the mesh density, but the ratio of σ_f to A_f can be arbitrary. This property can be utilized to enhance the computation speed when using the discrete fiber model in an explicit finite element code. In the explicit method, the maximum allowable time step is decreased as element stiffness is increased. Because in our model the greatest stiffness is found in the fibers, these will control the maximum time

Table 2 Simulation scales and configurations

Simulation	Feature size range	Reference configuration	Configurations simulated
Cell-scale	2–50 μ	Ω_2	Ω_2 – Ω_t
Tissue-scale	50 μ –1 mm	Ω_1	Ω_1 – Ω_t
Organ-scale	1 mm–3 cm	Ω_2	Ω_2 – Ω_t

step. In a one-dimensional element the maximum allowable time step is

$$\Delta t_{\max} = L \sqrt{\frac{\rho}{E}}, \quad (2)$$

where L is the length of the element, ρ is the density of the element, and E is the maximum material modulus (Hallquist 2006). The stiffness of a nonlinear cable element at a given strain ε_o

$$E = \left. \frac{\partial \sigma}{\partial \varepsilon} \right|_{\varepsilon=\varepsilon_o}. \quad (3)$$

As such, a fiber can be defined with artificially high cross-sectional areas A_f and corresponding artificially low stress σ_f . The resulting element will have low stiffness E , and thus allow large timesteps, while still giving the correct overall element stress σ_c .

The discrete fiber model was implemented in LS-DYNA. The constitutive model was constructed referring to the tissue configuration Ω_2 . The isotropic solid was modeled as a single-term Mooney-Rivlin with the value $C_1 = 2.0e4$ chosen to fit bending data for the leaflet (Gloeckner et al. 1999). The stress-strain curves in the radial and circumferential direction measured experimentally for configuration Ω_2 (Sacks and Yoganathan 2007) were discretized and applied to the fiber elements. Curves for σ_c were fit to the data and curves for σ_f were calculated using (Eq. 1) and a value of $1.0 \text{ e-}3 \text{ m}^2$ for A_f . The aortic root was assumed to be anisotropic and modeled with a single-term Mooney-Rivlin material. A value of $C_1 = 1.0e5$ was fit to experimental pressure-versus-dilation data for the root (Lansac et al. 2002).

Geometry of the AV was created in SolidWorks (SolidWorks, Concord MA). Separate loft features were used to represent the root and cusp. Dimensions were determined from collected measurements of the gross geometry (Thubrikar 1990) and varying cusp thicknesses (Grande-Allen et al. 2001). Cusps were positioned in an unloaded configuration that, according to observations of explanted valves made in our lab, best represents the unloaded configuration Ω_2 . Figure 3a shows the 3D geometry of the valve, with colors representing the separate loft features. Perfect symmetry of the valve was assumed so that only one-sixth of the valve needed to be considered for simulation. Entry regions were added both to allow the root to move freely while the portions of the wall at the inlet and outlet remain fixed to the stationary fluid sources. The solid domain consisting of valve, root, and entry regions was embedded in a cylindrical fluid domain with source regions representing fluid interface with the ventricle and aorta. Figure 3b shows the simulation geometry with 1/6 symmetry, entry regions, and fluid. Parametric 8-node brick meshes of both the solid and fluid domains were created in TrueGrid (XYZ Scientific Applications, Inc., Livermore CA). Figure 3c shows the meshed geometry.

Cable elements representing circumferential and radial fiber families were overlaid on the solid mesh using HyperMesh (Altair Engineering, Troy MI), following observed fiber directions (Sacks et al. 1998). The fiber families are illustrated in Fig. 4.

Fixities and boundary conditions were applied to the mesh. Mirror conditions were applied to fluid and solid nodes on the two symmetry planes. The unattached ends of the entry regions were fixed while the nodes at the junction

Fig. 3 (a) CAD geometry of whole valve, (b) CAD simulation geometry, (c) meshed geometry

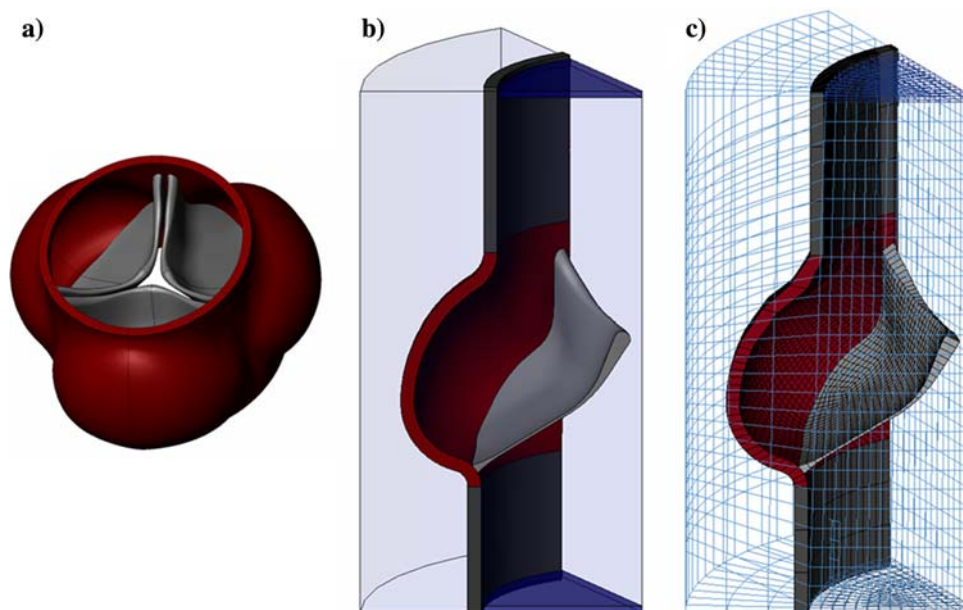


Fig. 4 One cusp, with (a) experimentally measured fiber orientation (Sacks et al. 1998) and (b) discrete fibers overlaid on the solid mesh. Red represents circumferential fibers and blue represents radial

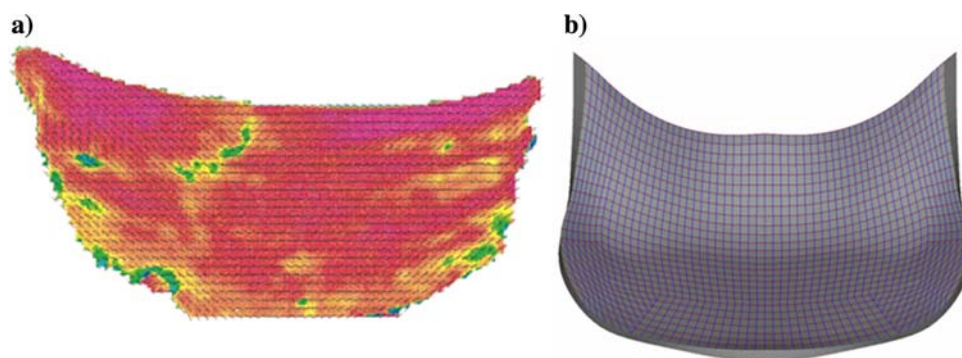
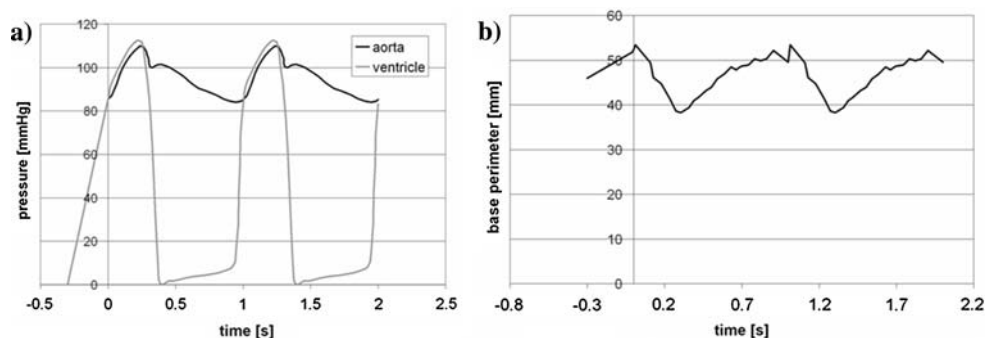


Fig. 5 (a) Pressure versus time curves applied as model boundary conditions, (b) Dilation of aortic valve base applied as model boundary condition



of the entry regions and the aortic root were constrained from moving axially. Outer faces of the fluid domain were not constrained.

Two cases were run in the organ-scale simulation, a static and a fully dynamic case. In the static case, constant pressures of 0, 1, 2, 4, 60, and 90 mmHg were applied at the aortic inlet sequentially. A settling time of 0.3 s was allowed at each pressure level. Pressure at the ventricular inlet was kept at 0 mmHg and ventricular contraction was not applied in the static case. In the dynamic case, measured time-varying pressures for the aorta and ventricle (Thubrikar 1990) were applied as boundary conditions to the fluid sources. The pressure values are plotted versus time in Fig. 5a. Contraction of the ventricle was represented by applying an experimentally-derived (Lansac et al. 2002) time-varying radial displacement to the base of the AV. The applied dilation of the base is plotted in Fig. 5b. In Fig. 5, the time from $-0.3 < t < 0$ represents the pressurization of the valve from configuration Ω_2 to Ω_3 . Configuration Ω_t is any state where $t > 0$. Systole occurs for approximately $0 < t < 0.25$ and diastole for $0.3 < t < 1.0$. All temporal plots in this paper are referred to this timeframe.

Results of the organ-level simulation were processed in HyperView (Altair Engineering, Troy MI). The model was verified by comparing a number of behaviors in the solid and fluid to experimental data. Element deformations were tracked at three locations for mapping to the tissue-level simulation. These three locations are illustrated in Fig. 6.

Tissue-level Simulation

In the organ-level simulation, we use a greatly simplified model of the cusp tissue. This simplified model gives the

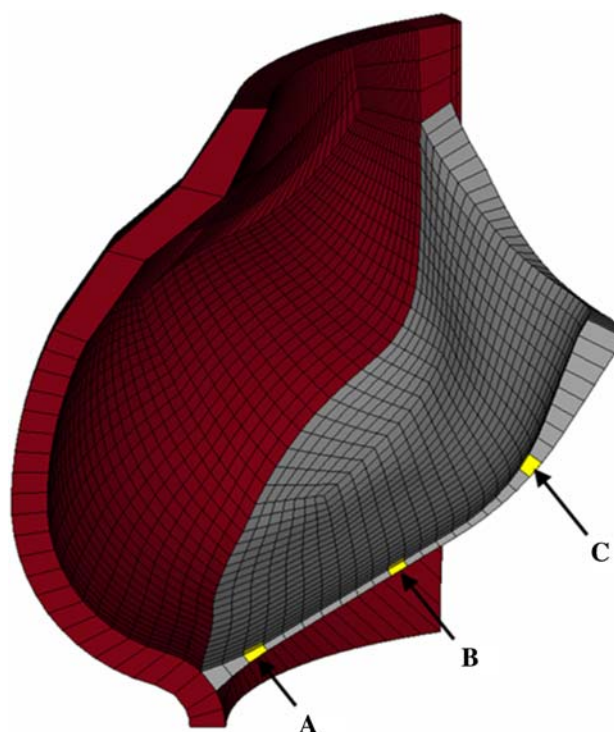


Fig. 6 Locations to track deformations in the organ-scale simulation

correct bulk behavior (bending and biaxial stiffness), but does not predict local tissue deformations. To do so, we developed a tissue model that incorporates all of the major known features of the cusp tissue. These characteristics are: the cusp has three distinct layers (the ventricularis, spongiosa, and fibrosa), the fibrosa and ventricularis have embedded families of aligned fibers, the fibrosa is highly undulated, and the spongiosa is gel-like.

We created the tissue-level model in the ADINA implicit finite-element software (ADINA R&D, Watertown MA). Computational cost is not a concern so, unlike in the organ-scale model, we can use continuum material models. We consider the fibrous layers to be composed of an isotropic exponential material with a family of embedded exponential fibers running in the circumferential tissue direction. Additionally, bending data (Gloeckner et al. 1999) show that the tissue has an initial modulus.

We model the isotropic exponential material with a single-term Fung-like exponential (Fung 1993). The strain energy function for this term is

$$W_{\text{exponential}} = C_{1m} \{ \exp [C_{2m}(I_1 - 3)] - 1 \}, \tag{4}$$

where C_{1m} and C_{2m} are constants that will be calculated from experimental data and I_1 is the first strain invariant. We provide an initial modulus with a single-term Mooney-Rivlin, for which the strain energy function is

$$W_{\text{initial}} = C_I(I_1 - 3), \tag{5}$$

where C_I is a constant that will be calculated from experimental data. The embedded fiber family is modeled using the Holzapfel model (Holzapfel et al. 2000),

$$W_{\text{fiber}} = \frac{C_{1f}}{2C_{2f}} \left\{ \exp \left[C_{2f}(I_4 - 3)^2 \right] - 1 \right\}, \tag{6}$$

where C_{1f} and C_{2f} are constants that will be calculated from experimental data. The complete strain energy function for a fibrous layer is a sum of the terms above,

$$W = C_{1m} \{ \exp [C_{2m}(I_1 - 3)] - 1 \} + C_I(I_1 - 3) + \frac{C_{1f}}{2C_{2f}} \left\{ \exp \left[C_{2f}(I_4 - 3)^2 \right] - 1 \right\}. \tag{7}$$

We modeled the spongiosa with a single-term Mooney-Rivlin strain energy function.

The fiber layers are described by five constants: C_I , C_{1m} , C_{2m} , C_{1f} , and C_{2f} . We calculate these values from experimental data. Sensitive measurements of the tissue flexural stiffness simply give the initial modulus. We assume that the initial modulus is the same in the ventricularis and fibrosa and that the stiffness of the spongiosa, which is much more compliant (Vesely and Noseworthy 1991), is an order of magnitude lower.

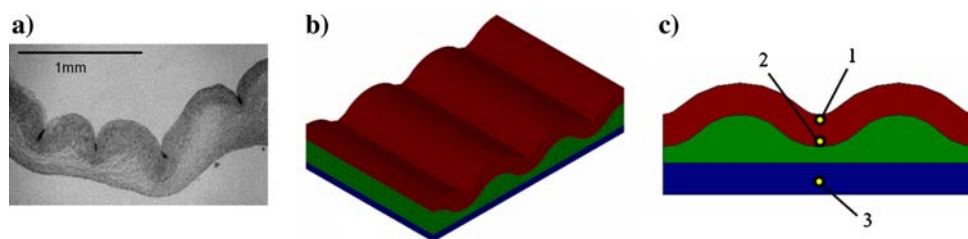
Constants of the exponential terms were determined from biaxial stress-strain data for the individual layers (Sacks and Yoganathan 2007). Two values were extracted for both the radial and circumferential tissue directions. A locking modulus E_L is defined as the Young’s modulus in the direction of interest when the tissue reaches full extensibility in that direction. The extensibilities and locking moduli in the circumferential and radial directions are adequate to analytically solve for the four remaining constants, C_{1m} , C_{2m} , C_{1f} , and C_{2f} . The extensibilities, moduli, and determined constants, are listed in Table 3. We have calculated the constants referred both to configuration Ω_0 and Ω_1 .

Geometry for the model of assembled tissue, configuration Ω_1 , was created in Solidworks. The dimensions are based on measurements of tissue thickness (Sacks and Yoganathan 2007; Vesely and Noseworthy 1991) and observations of tissue cross-sections. Figure 7a shows a micrograph cross-section of valve cusp tissue, and Fig. 7b, the meshed CAD representation of this geometry. Material properties from Table 3 were assigned to the appropriate layers in configuration Ω_1 . Biaxial stress and bending conditions were applied to the assembled tissue, and the results were compared to experimental data (Billiar and Sacks 2000a, Gloeckner et al. 1999). Each term in (Eq. 7) is convex over a wide range of deformations, so the complete equation was also expected to maintain convexity. We examined convexity on the ventricularis and fibrosa models by calculating the strain energy over a wide range of biaxial conditions.

Table 3 Tissue layers and properties in configurations Ω_0 and Ω_1

Layer	Configuration	Extensibility		Locking modulus		C_I [Pa]	C_{1m} [Pa]	C_{2m} [-]	C_{1f} [Pa]	C_{2f} [-]
		Circumferential [-]	Radial [-]	Circumferential [Pa]	Radial [Pa]					
Fibrosa	Ω_0	1.1	1.4	2.6e7	1.1e7	2.0e4	0.95	1.4e3	0.04	24
	Ω_1	1.1	1.4	2.6e7	1.1e7	2.0e4	0.95	1.4e3	0.04	24
Ventricularis	Ω_0	1.2	1.9	1.6e7	5.0e6	2.0e4	2.5e-5	1.1e2	0.04	5.4
	Ω_1	1.2	1.7	1.6e7	5.0e6	2.0e4	2.5e-5	1.1e2	0.05	5.7

Fig. 7 (a) micrograph of AV leaflet cross-section (Sung et al. 1999), (b) meshed model of AV leaflet, (c) locations for deformation tracking



We used the model of the multilayered tissue referred to configuration Ω_1 to map deformations from the organ-scale model to the cell-scale model. First, a radial stretch is applied to move the tissue from configuration Ω_1 to Ω_2 , its position in the unpressurized valve. Then element strains measured in the organ-level simulation, which covers configurations Ω_2 through Ω_t , were applied as time-varying displacement boundary conditions to the tissue model. Deformations at points within the ventricularis and fibrosa, shown in Fig. 7c, were tracked and passed on to the cell-level simulation. Point 1 is in an expected high-deformation region of the fibrosa, Point 2 is in an expected low-deformation region of the fibrosa, and Point 3 is in the ventricularis. Mapping was performed for both the static and dynamic cases.

In addition to the model of the multilayered tissue, we have modeled the assembly of the tissue (transition from Ω_0 to Ω_1) with the observed preloading between fibrosa and ventricularis (Vesely 1996; Vesely and Lozon 1993). A model fibrosa with mechanical properties referred to Ω_0 was compressed and a fibrosa stretched using the values plotted in Table 3. While this model was not used in our current multiscale approach, it does allow prediction of deformations over the entire range from Ω_0 to Ω_t .

Cell-level Simulation

The cell-level simulation consists of a single cell surrounded by matrix, either fibrosa or ventricularis. Constitutive models for the matrix are the same as those for the tissue-level model. The constitutive model for the cell is a single-term Mooney-Rivlin with $C_I = 400$ Pa (Huang 2004).

Geometry was created in ADINA (ADINAR&D, Watertown MA). A sphere was created within cube and then scaled in the three dimensions to give the cell an ellipsoidal shape. According to experimental measurements (Huang 2004), the major axes of this cell were defined to be $10\ \mu\text{m}$ in the circumferential direction, $7.7\ \mu\text{m}$ in the radial direction, and $4.3\ \mu\text{m}$ in the transmural direction. Three planes of symmetry were defined so that the computation domain consists of 1/8th of the cell and matrix. The simulation geometry is shown in Fig. 8.

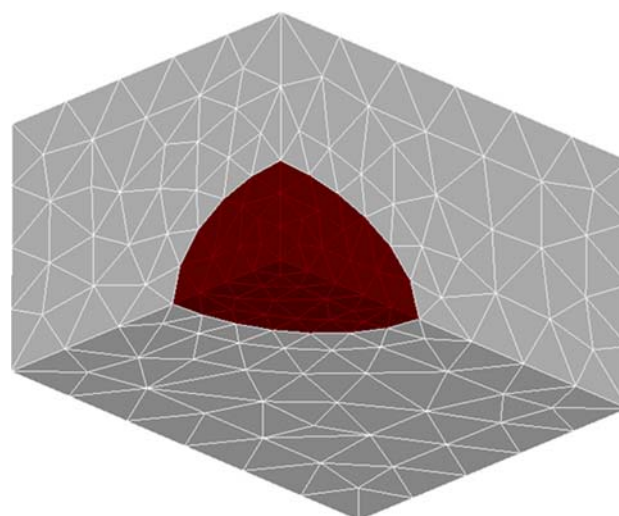


Fig. 8 Meshed geometry for cell-scale simulation. Cell is colored red and matrix is gray

Displacement boundary conditions were applied to the outer faces of the matrix. These displacements were defined to represent the element strains calculated in the tissue-level simulation. Because the relevant experiments (Huang 2004) start with the valve in a zero-pressure state, we started our cell simulations in the unpressurized valve configuration Ω_2 . Cell aspect ratio (CAR) was output from the simulation. The model was verified by comparing results of the static case to experimental CAR measurements made under the same conditions (Huang 2004). Cell aspect ratio was also computed for the dynamic case of valve opening and closing.

Results

Organ-level Simulation

The discrete fiber constitutive model was found to be adequate in predicting the bulk deformation behavior of the tissue. Figure 9a shows the biaxial response of this model and Fig. 9b shows the bending response. Because we are not aware of any experimental data for tissue properties referred to the assembled valve configuration Ω_2 , we could not construct this model to match a specific case. Note,

Fig. 9 Discrete fiber model predictions and experimental results: (a) predicted biaxial behavior and experimental data for a lightly preloaded case (Billiar and Sacks 2000a), (b) predicted bending behavior and the experimental data (Sacks 2001) to which the model was fit

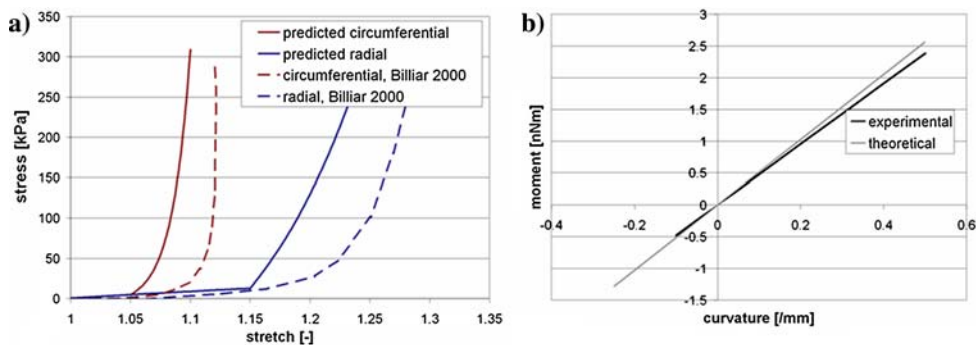
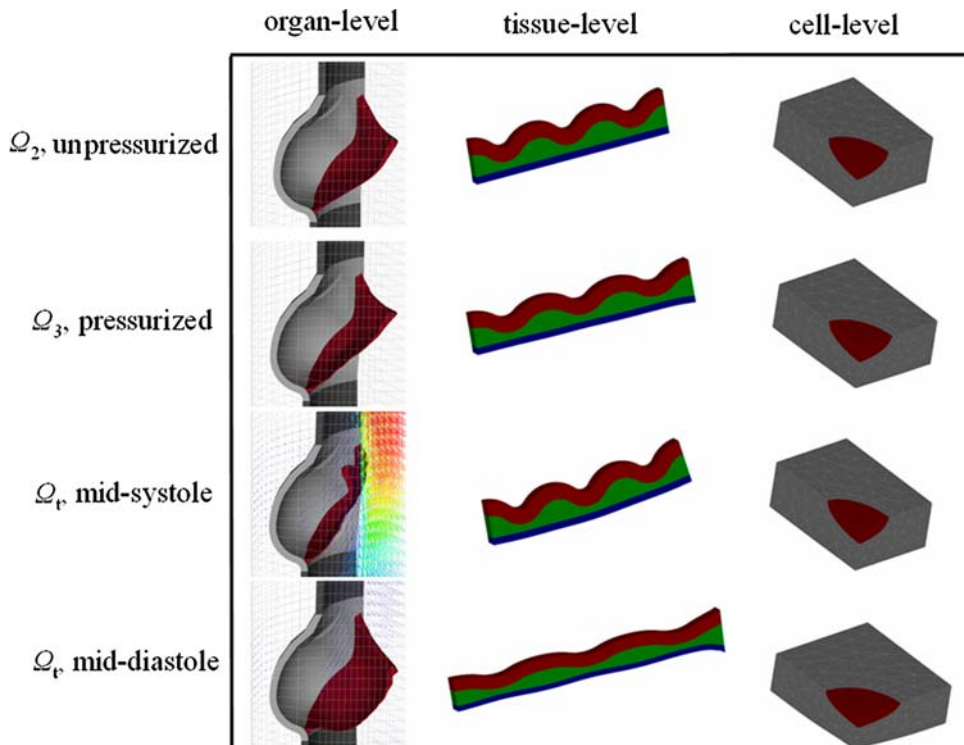


Fig. 10 Selected deformed states in each dynamic simulation



however, in Fig. 9a the similarity between our model predictions and the measurements made by Billiar referred to a lightly preloaded configuration (Billiar and Sacks 2000a). This enforces the notion that the tissue exists in a lightly preloaded state in the valve.

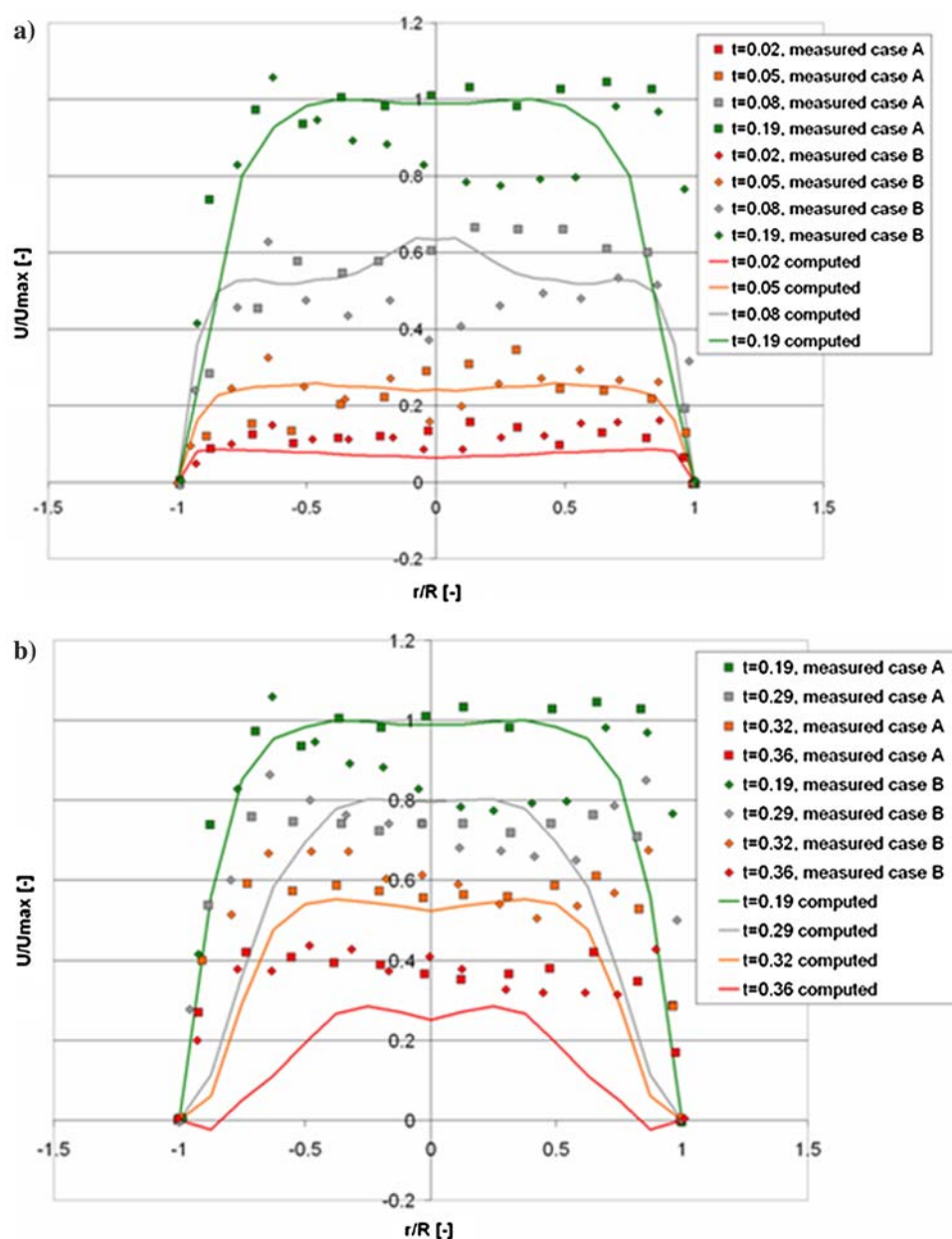
One second of physical time, representing either the full static case or one dynamic cycle of valve opening and closing, ran in approximately 3 h of computation time on a workstation with 4 Xeon 5160 3.00 GHz processors. There was no leakage in the fluid-structure interaction, and the cusps coapted and sealed against flow. Figure 10a shows the valve in various stages of the dynamic cycle.

For the dynamic case, theoretical predictions matched experimental data in a number of measures. In the fluid phase, the bulk flow rate through the valve closely corresponded with experimental data (Nichols and O'Rourke 1998). Velocity profiles predicted at various times across

the AV outlet are compared to experimental measurements in Fig. 11. Theoretical and measured flow rates are plotted versus time in Fig. 12. In the solid phase, predictions were compared to experimental data for cusp edge and center displacement, circumferential strain, radial strain, and root motion (Thubrikar 1990). These results are plotted in Fig. 13. In the fluid and solid phase, predictions display all major trends with correct magnitudes when compared to measured data. Error magnitudes are acceptable given patient-to-patient variation, beat-to-beat variation, and experimental errors inherent in measurement of the rapidly moving in-vivo system.

Element stretches averaged over the locations illustrated in Fig. 6 for the static case are shown in Fig. 14. Deformations recorded in the dynamic case for location B shown in Fig. 6 in the dynamic case are plotted versus time in Fig. 15. Stretches for $t < 0$ represent the unknown

Fig. 11 Predicted and measured velocity profiles at AV exit: (a) shows profiles while the fluid is accelerating flow and (b) during deceleration



stretches between reference configurations Ω_2 and Ω_3 discussed in Section “Multi-Scale Approach”. The dominant deformations were the tensile stretches in the radial and circumferential directions and the bending in the radial direction. In the tracked locations, shears in and out of the plane of the tissue as well as bending in the circumferential direction tended to be small and were not mapped to the tissue-level model.

Tissue-level Simulation

All tissue-level simulations ran to convergence over a range of strains larger than is expected to be seen

physiologically. Contour plots of the strain-energy surfaces for the fibrosa and ventricularis models are shown in Fig. 16. For visualization of the wide variation in energies of these exponential functions, we have plotted $\log(W)$. Convexity was maintained in all tested cases. The responses of the fibrosa and ventricularis model to biaxial tension are plotted in Fig. 17. The predicted biaxial and bending behaviors of the complete tissue model compared to experimental (Gloeckner et al. 1999; Sacks and Yoganathan 2007) are shown in Fig. 18. We note a discrepancy in the experimental data for the circumferential direction between the individual layers (Fig. 17) (Sacks and Yoganathan 2007) and the assembled tissue (Fig. 18) (Billiar and Sacks 2000a): the assembled tissue is more extensible

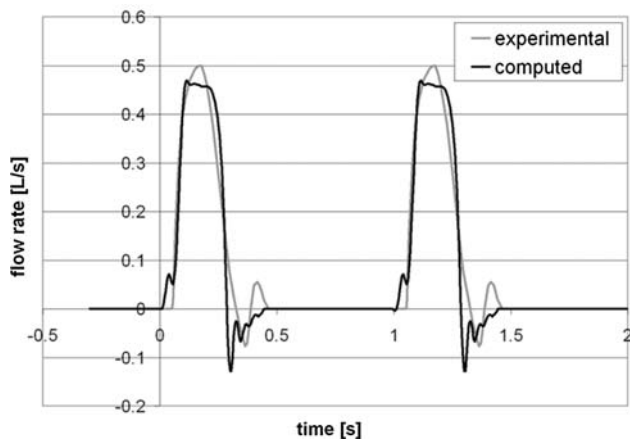


Fig. 12 Predicted and measured flow rates through AV

than the fibrosa in this direction. Hence, our model matches the data for individual layers well and underestimates the extensibility of the assembled tissue compared to this data set. The smaller value of the extensibility is consistent with stretches observed in the functioning valve (Cataloglu et al. 1976, 1977; Thubrikar et al. 1986).

Radial stretches due to assembly of the layers into a complete tissue (deforming from Ω_0 to Ω_1) are shown in Fig. 19. Deformation states for the tissue model subject to strains measured in the organ-level model are shown at various times in Fig. 10b. Stretch magnitudes predicted in the static case are plotted in Fig. 20. Stretches recorded in the tissue model for the dynamic case are plotted versus time in Fig. 21.

Cell-level Simulation

All cell-level simulations ran to convergence. Deformation states for selected locations at various times in the cycle are illustrated in Fig. 10c. In Fig. 22, cellular aspect ratios predicted for the static case are compared to measurements (Huang 2004) made under static pressure. Values at points 1, 2, and 3 are plotted. The experimental data is an average over the leaflet, so we have also plotted the average over points 1, 2, and 3. The variation in CAR through the leaflet thickness and with varying pressure is compared to experimental data (Huang 2004) in Fig. 23. In both comparisons, the predictions closely match the experimental data. In the dynamic case, we have computed the time-varying aspect ratios for the three points tracked in the tissue-scale simulation at the three locations tracked in the organ-scale simulation for a total of 9 points. To give a typical response, we have averaged together the cellular aspect ratios for point 1 (see Fig. 7c.) of locations A, B, and C (see Fig. 6). We have done the same for points 2 and 3. The results are plotted in Fig. 24.

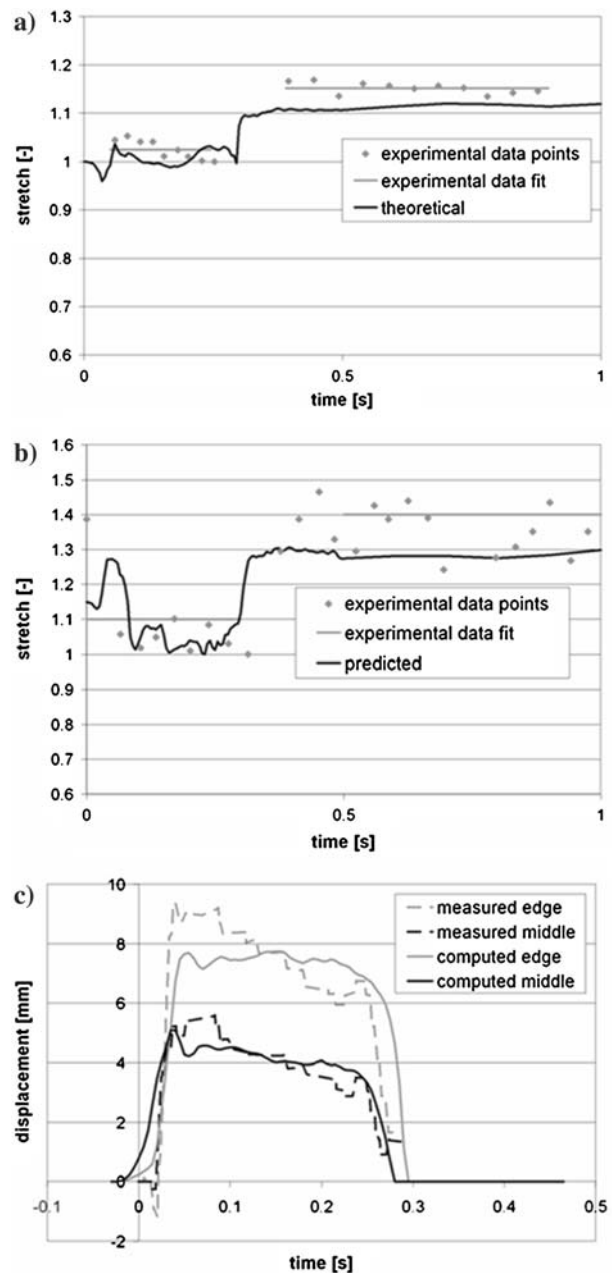


Fig. 13 Predicted and measured (Thubrikar 1990) motion of valve leaflets: (a) circumferential leaflet stretch, (b) radial leaflet stretch, (c) displacement of points at edge and middle of leaflet

Discussion

Organ-level Simulation

A number of assumptions were made to simplify analysis of the valve motion. First, a 1/6 symmetry was assumed for the valve. In reality, there is at least a difference between the coronary and non-coronary sinuses and cusps. It has been shown that the asymmetry does create different strain states in leaflets of the same valve (Grande et al. 1998).

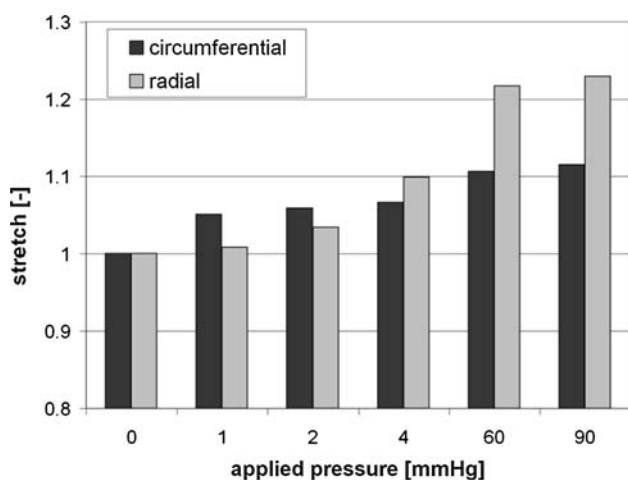


Fig. 14 Element stretches predicted in static case

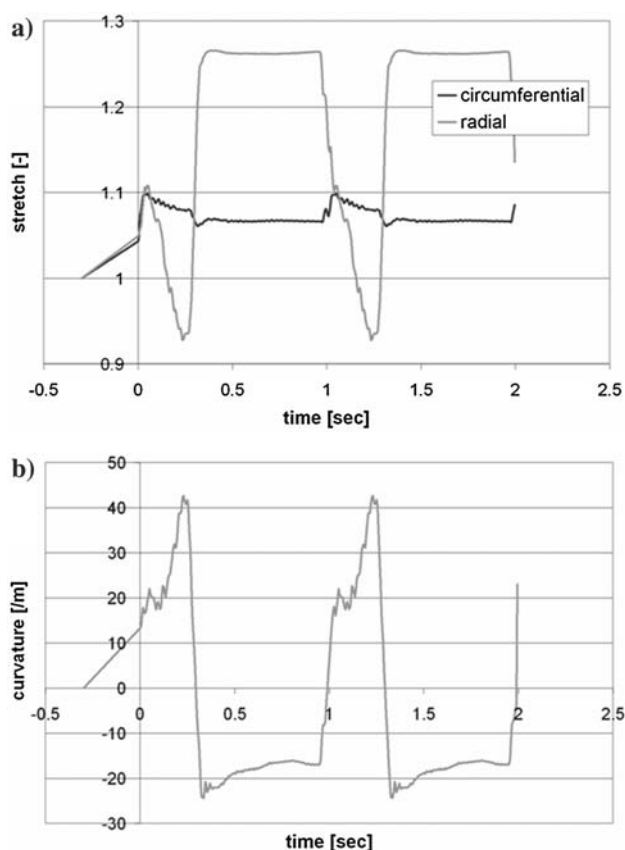


Fig. 15 Element deformations predicted in dynamic case versus time: (a) planar stretches, (b) curvature

However, these differences are small relative to the large displacements and strains that take place in the valve. The experiments to which we have compared our predictions generally do not note a difference between leaflets (Thubrikar 1990), hence the effects of asymmetry are finer than the current work can resolve. A coarse mesh was used, particularly in the fluid phase, to decrease computation

time. Prediction of finer features of the fluid and shears within thin boundary layers would require a significantly refined mesh.

Equally important simplifications were made in the choice of material model used. We assumed that both the leaflet and wall materials are homogenous and that the leaflet fiber directions can be represented simply by two fiber families. Both the leaflet (Sacks et al. 1998) and wall (Lansac et al. 2002) have been shown to be inhomogeneous, and the leaflet fiber distribution varies throughout the leaflet and changes as the tissue deforms (Sacks et al. 1998). There does not currently exist, however, a complete map of material properties to the valve geometry. For example, the leaflet material properties have been accurately measured in-vitro (Billiar and Sacks 2000a), but the effects of physical preloads and cellular contraction (Merryman et al. 2006a) in-vivo are undetermined. The discrete-fiber model simulates the main features that we currently understand to be important to the tissue bulk deformation.

Other simplifications include our smooth CAD representation of a complex biological geometry, representation of the ventricular contraction as a simple displacement condition, and lack of tissue surrounding the aortic root. The organ-scale model is clearly an idealization of the physical case. Comparison of the model to experimental data for both the fluid and solid domains shows that the model capably represents the valve motion in both domains.

Tissue-level Simulation

The purpose of the tissue-level simulation is to translate deformations from the organ scale to the cell scale. Since the AV cusp tissue is multilayered and undulated, the tissue model must also have those characteristics in order to accurately predict the cell-level deformations. While the bulk properties of the tissue have been widely reported, the details of the interplay between layers and motion of the undulations in the fibrosa as the tissue deforms are not known. Our tissue model simulates the major bulk behaviors of each layer and of the complete tissue but the local behaviors are, at this time, speculative. Experimental investigation into the local deformations of the AV tissue could be used to verify this work. Currently, the tissue model accurately represents bulk tissue behavior and approximates local behavior to the highest resolution possible given available knowledge.

Cell-level Simulation

Our model of the mechanics of VICs in the leaflets is highly simplified. Both the matrix and cell are modeled as

Fig. 16 Contour plots of $\log(W)$ for continuum model subjected to biaxial loading conditions: (a) fibrosa model, (b) ventricularis model

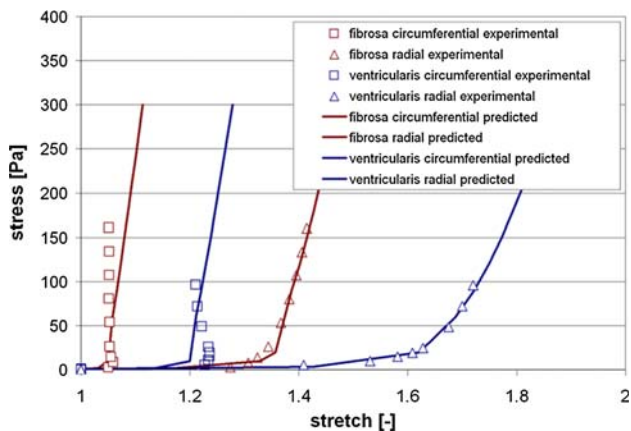
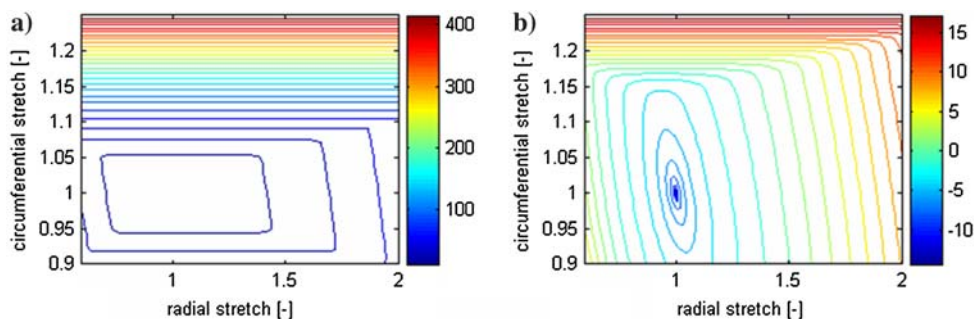


Fig. 17 Predictions and experimental (Sacks and Yoganathan 2007) data for biaxial tension of individual layers, referred to configuration Ω_0

Fig. 18 Continuum model predictions for the assembled tissue, referred to configuration Ω_1 , compared to experimental results (Billiar and Sacks 2000a; Gloeckner et al. 1999): (a) biaxial, (b) bending

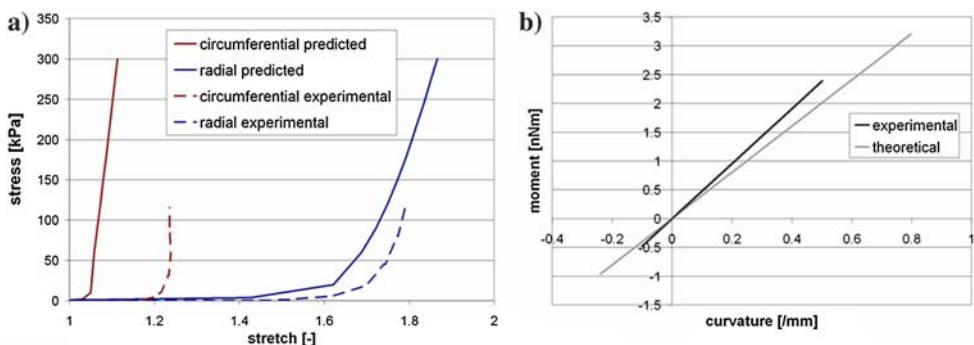
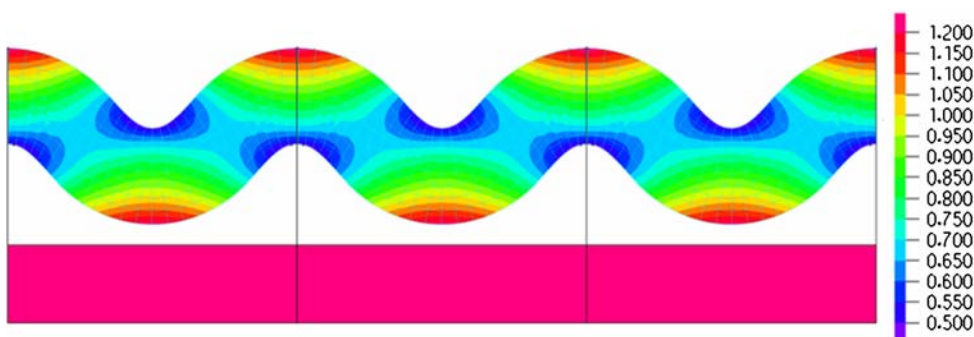


Fig. 19 Radial stretches due to assembling layers into complete tissue



homogenous solids. Actually, the fibrous nature of the matrix is evident at the cell scale and the cell has multiple solid and fluid components. The features of the matrix and cell have not been determined beyond what we have included in our model, though. Given the series of assumptions made across the simulations, the predictive ability of the cell-level simulation demonstrated in the static case is remarkable. Our model predicts both the trend and magnitude of change in CAR with pressure as well as the variation across the leaflet thickness. These results give a high degree of confidence in the predictions for the dynamic case.

Conclusions

We have created three models for AV mechanics, one at each of the cell, tissue, and organ length scales. The

Fig. 20 Stretch magnitudes predicted by tissue-scale model for static case: (a) circumferential, (b) radial

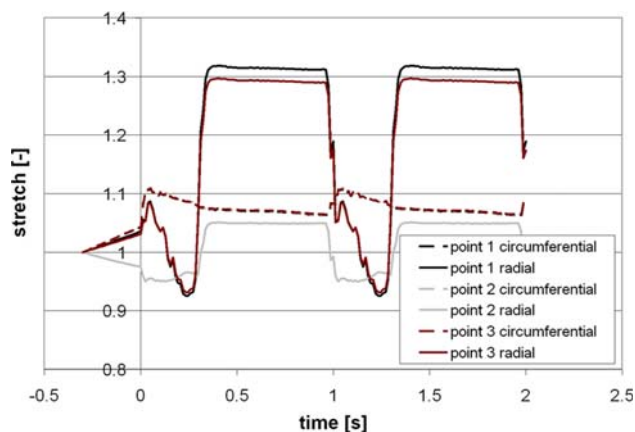
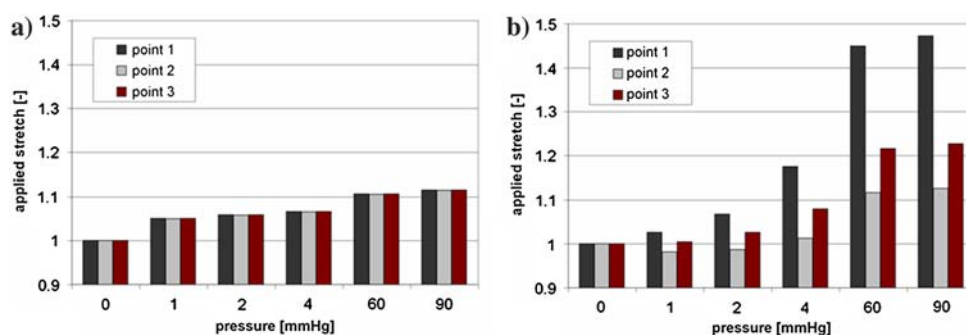


Fig. 21 Stretch magnitudes predicted by tissue-scale model versus time at location B illustrated in Fig. 6 for the dynamic case

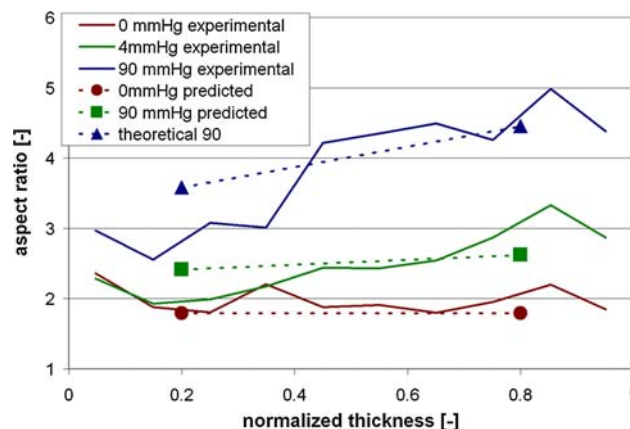


Fig. 23 Predicted distribution of cellular aspect ratios through leaflet thickness compared to experimental measurements (Huang 2004) for the static case. Normalized thickness varies from the ventricularis surface at 0 to the fibrosa surface at 1

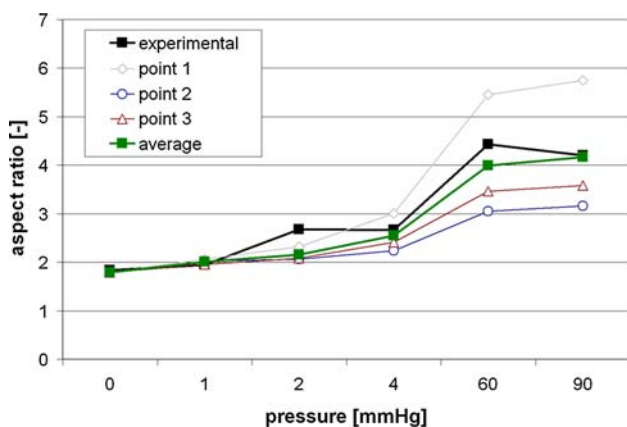


Fig. 22 Predicted cellular aspect ratios compared to experimental measurements (Huang 2004) for the static case

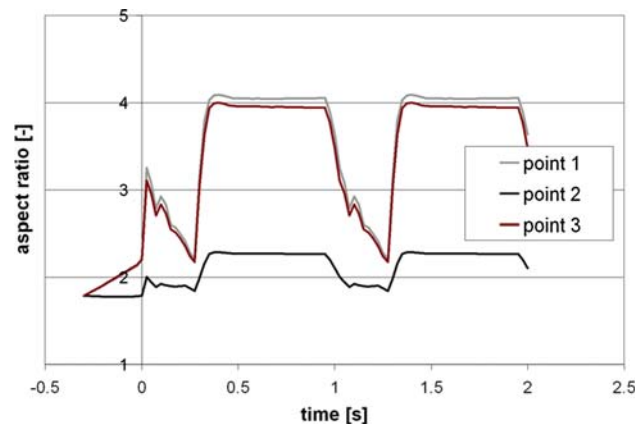


Fig. 24 Predicted cellular aspect ratios for the dynamic case, averaged over organ-scale locations A, B, and C

individual models capture the major known mechanical aspects at their respective scales. We have demonstrated that each model is numerically functional and satisfactorily matches experimental data. Each model represents a significantly simplified version of the physical AV, and they all can be refined by coordinating with further experimental work.

We have introduced a coherent set of reference configurations to link the three models so as to create one multiscale simulation of the complete mechanics and motion of the AV. We have verified our multiscale model in the static case, which simulates a multiscale experiment that has been previously performed. In this case, the input

to the model is made at the organ scale (pressure boundary conditions). Deformations pass through the length scales and the output is observed at the cell scale (cell aspect ratios). We have demonstrated the ability of our approach to accurately handle the multiscale behavior in the static case, providing confidence in the predictions for the dynamic case.

Our multiscale model has application in studying both the healthy and diseased AV. In particular, the disease calcific aortic stenosis has a multiscale mechanical pathology. One of the causes of CAS is understood to be abnormal tissue strains giving rise to abnormal VIC responses, leading to calcification. This process can be examined using the multiscale model we have presented. The effect of the disease is a stiffening of the matrix material, and our model can simulate stiffening at all three length scales. We expect that multiscale simulation of the AV will be a valuable tool to be used along side experimental work to better understand AV health and disease.

References

- Baumert B, Plass A, Bettex D, Alkadhi H, Desbiolles L, Wildermuth S, Marincek B, Boehm T. Dynamic cine mode imaging of the normal aortic valve using 16-channel multidetector row computed tomography. *Invest Radiol* 2005;40:637–47.
- Billiar K, Sacks MS. Biaxial mechanical properties of the natural and glutaraldehyde treated aortic valve cusp-Part I: experimental results. *J Biomech Eng* 2000a;122:23–30.
- Billiar K, Sacks MS. Biaxial mechanical properties of the natural and glutaraldehyde treated aortic valve cusp-Part II: a structural constitutive model. *J Biomech Eng* 2000b;122:327–35.
- Boehm T, Husmann L, Leschka S, Desbiolles L, Marincek B, Alkadhi H. Image quality of the aortic and mitral valve with CT: relative versus absolute delay reconstruction. *Acad Radiol* 2007;14:613–24.
- Brewer RJ, Mentzer RM, Deck JD, Ritter RC, Trefil JS, Nolan SP. In vivo study of dimensional changes of aortic-valve leaflets during cardiac cycle. *J Thorac Cardiovasc Surg* 1977;74:645–50.
- Cataloglu A, Clark R, Gould P. Stress analysis of aortic valve leaflets with smoothed geometrical data. *J Biomech* 1977;10:153.
- Cataloglu A, Gould P, Clark R. Refined stress analysis of human aortic heart valves. *J Eng Mech Div Proc Am Soc Civil Eng* 1976;102:135–50.
- Chandran PL, Barocas VH. Deterministic material-based averaging theory model of collagen gel micromechanics. *J Biomech Eng-T ASME* 2007;129:137–47.
- Clark RE, Karara SM, Catalogl A, Gould PL. Determination of diastolic stresses in human aortic-valve through close range stereophotogrammetry. *Circulation* 1974;50:165–5.
- De Hart J, Baaijens FPT, Peters GWM, Schreurs PJG. A computational fluid-structure interaction analysis of a fiber-reinforced stentless aortic valve. *J Biomech* 2003a;36:699–712.
- De Hart J, Peters GWM, Schreurs PJG, Baaijens FPT. A three-dimensional computational analysis of fluid-structure interaction in the aortic valve. *J Biomech* 2003b;36:103–12.
- De Hart J, Peters GWM, Schreurs PJG, Baaijens FPT. Collagen fibers reduce stresses and stabilize motion of aortic valve leaflets during systole. *J Biomech* 2004;37:303–11.
- Deck JD, Thubrikar MJ, Schneider PJ, Nolan SP. Structure, stress, and tissue-repair in aortic-valve leaflets. *Cardiovasc Res* 1988;22:7–16.
- Einstein DR, Kunzelman KS, Reinhall PG, Nicosia MA, Cochran RP. Haemodynamic determinants of the mitral valve closure sound: a finite element study. *Med Biol Eng Comput* 2004;42:832–46.
- Einstein DR, Kunzelman KS, Reinhall PG, Nicosia MA, Cochran RP. Non-linear fluid-coupled computational model of the mitral valve. *J Heart Valve Dis* 2005;14:376–85.
- Fung Y. *Biomechanics: mechanical properties of living tissues*. New York: Springer; 1993.
- Gloeckner D, Billiar K, Sacks M. Effects of mechanical fatigue on the bending properties of the porcine bioprosthetic heart valve. *ASAIO J* 1999;45:59–63.
- Gould P, Cataloglu A, Dhatt G, Cattopadhyay A, Clark R. Stress analysis of the human aortic valve. *Comput Struct* 1973;3:377.
- Grande-Allen K, Cochran R, Reinhall P, Kunzelman K. Finite-element analysis of aortic valve sparing: influence of graft shape and stiffness. *IEEE Trans Biomed Eng* 2001;48:647–59.
- Grande KJ, Cochran RP, Reinhall PG, Kunzelman KS. Stress variations in the human aortic root and valve: the role of anatomic asymmetry. *Ann Biomed Eng* 1998;26:534–45.
- Hallquist J. *LS-DYNA theory manual*. Livermore; 2006.
- Holzappel GA, Gasser TC, Ogden RW. A new constitutive framework for arterial wall mechanics and a comparative study of material models. *J Elast* 2000;61:1–48.
- Huang H-YS. *Micromechanical simulations of heart valve tissues*: University of Pittsburgh; 2004.
- Humphrey JD. *Continuum biomechanics of soft biological tissues*. Proceedings of the Royal Society of London Series A—Mathematical Physical and Engineering Sciences 2003;459:3–46.
- Kim H, Chandran KB, Sacks MS, Lu J. An experimentally derived stress resultant shell model for heart valve dynamic simulations. *Ann Biomed Eng* 2007;35:30–44.
- Kim H, Lu J, Sacks MS, Chandran KB. Dynamic simulation pericardial bioprosthetic heart valve function. *J Biomech Eng-T ASME* 2006;128:717–24.
- Lansac E, Lim HS, Shomura Y, Lim KH, Rice NT, Goetz W, Acar C, Duran CMG. A four-dimensional study of the aortic root dynamics. *Eur J Cardiothorac Surg* 2002;22:497–503.
- Lim C, Zhou E, Quek S. Mechanical models for living cells—a review. *J Biomech* 2006;39:195–216.
- Merryman WD, Huang H-YS, Schoen FJ, Sacks MS. The effects of cellular contraction on aortic valve leaflet flexural stiffness. *J Biomech* 2006a;39:88–96.
- Merryman WD, Youn I, Lukoff HD, Krueger PM, Guilak F, Hopkins RA, Sacks MS. Correlation between heart valve interstitial cell stiffness and transvalvular pressure: implications for collagen biosynthesis. *Heart Circ Physiol* 2006b;290:H224–31.
- Migliavacca F, Balossino R, Pennati G, Dubini G, Hsia TY, de Leval MR, Bove EL. Multiscale modelling in biofluidynamics: Application to reconstructive paediatric cardiac surgery. *J Biomech* 2006;39:1010–20.
- Mofrad MRK, Kamm RD, editors. *Cytoskeletal mechanics: models and measurements*. Cambridge University Press; 2006.
- Nichols W, O'Rourke M. *McDonald's blood flow in arteries*. 5th ed. London: Arnold; 1998.
- Nicosia MA, Cochran RP, Einstein DR, Rutland CJ, Kunzelman KS. A coupled fluid-structure finite element model of the aortic valve and root. *J Heart Valve Dis* 2003;12:781–9.
- Otto CM. Calcification of bicuspid aortic valves. *Heart* 2002;88:321–2.
- Rousseau EPM, Sauren A, Vanhout MC, Vansteenhoven AA. Elastic and viscoelastic material behavior of fresh and

- glutaraldehyde-treated porcine aortic-valve tissue. *J Biomech* 1983;16:339–48.
- Sacks MS. The biomechanical effects of fatigue on the porcine bioprosthetic heart valves. *J Long Term Effects Med Implants* 2001;11(3–4):231–47.
- Sacks MS, Smith DB, Hiester ED. The aortic valve microstructure: effects of transvalvular pressure. *J Biomed Mater Res* 1998;41:131–41.
- Sacks MS, Yoganathan AP. Heart valve function: a biomechanical perspective. *Phil Trans R Soc B* 2007;362:1369–91.
- Stella JA, Sacks MS. On the biaxial mechanical properties of the layers of the aortic valve leaflet. *J Biomech Eng* 2007; in press.
- Sun W, Abad A, Sacks MS. Simulated bioprosthetic heart valve deformation under quasi-static loading. *J Biomech Eng-T ASME* 2005;127:905–14.
- Sun W, Sacks MS. Finite element implementation of a generalized Fung-elastic constitutive model for planar soft tissues. *Biomech Model Mechanobiol* 2005;4:190–9.
- Sung H-W, Chang Y, Chui C-T, Chen C-N, Liang H-C. Mechanical properties of a porcine aortic valve fixed with a naturally occurring crosslinking agent. *Biomaterials* 1999;20:1759–72.
- Taylor P, Batten P, Brand N, Thomas P, Yacoub M. The cardiac valve interstitial cell. *Int J Biochem Cell Biol* 2003;35:113–8.
- Thubrikar M. The aortic valve. Boca Raton: CRC Press; 1990.
- Thubrikar M, Piepgrass WC, Deck JD, Nolan SP. Stresses of natural versus prosthetic aortic-valve leaflets *in vivo*. *Ann Thorac Surg* 1980;30:230–9.
- Thubrikar MJ, Nolan SP, Aouad J, Deck JD. Stress sharing between the sinus and leaflets of canine aortic valve. *Ann Thorac Surg* 1986;42:434–40.
- Vesely I. Reconstruction of loads in the fibrosa and ventricularis of porcine aortic valves. *ASAIO J* 1996;42:M739–46.
- Vesely I, Lozon A. Natural preload of aortic valve leaflet components during glutaraldehyde fixation: effects on tissue mechanics. *J Biomech* 1993;26:121–31.
- Vesely I, Noseworthy R. Micromechanics of the fibrosa and the ventricularis in aortic valve leaflets. *J Biomech* 1991;25:101–13.
- Weinberg EJ, Kaazempur-Mofrad MR. A large-strain finite element formulation for biological tissues with application to mitral valve leaflet tissue mechanics. *J Biomech* 2005;39:1557–61.
- Weinberg EJ, Kaazempur-Mofrad MR. A finite shell element for heart mitral valve leaflet mechanics, with large deformations and 3D constitutive model. *J Biomech* 2006;40:705–11.